Microsc. Microanal. 22, 208–218, 2016
doi:10.1017/S1431927615015706

Microscopy AND Microanalysis

Automatic Detection of Pearlite Spheroidization Grade of Steel Using Optical Metallography

Naichao Chen,[1,2,*] Yingchao Chen,[1] Jun Ai,[1] Jianxin Ren,[1] Rui Zhu,[1] Xingchi Ma,[1] Jun Han,[3] and Qingqian Ma[3]

[1]*School Energy and Mechanical Engineering, Shanghai University of Electric Power, Shanghai 200090, China*
[2]*Shanghai Key Laboratory of Materials Protection and Advanced Materials in Electric Power, Shanghai 200090, China*
[3]*Shanghai Special Equipment Inspection and Research Institute, Shanghai 200333, China*

Abstract: To eliminate the effect of subjective factors during manually determining the pearlite spheroidization grade of steel by analysis of optical metallography images, a novel method combining image mining and artificial neural networks (ANN) is proposed. The four co-occurrence matrices of angular second moment, contrast, correlation, and entropy are adopted to objectively characterize the images. ANN is employed to establish a mathematical model between the four co-occurrence matrices and the corresponding spheroidization grade. Three materials used in coal-fired power plants (ASTM A315-B steel, ASTM A335-P12 steel, and ASTM A355-P11 steel) were selected as the samples to test the validity of our proposed method. The results indicate that the accuracies of the calculated spheroidization grades reach 99.05, 95.46, and 93.63%, respectively. Hence, our newly proposed method is adequate for automatically detecting the pearlite spheroidization grade of steel using optical metallography.

Key words: pearlite spheroidization, grade, optical metallography, image mining, artificial neural networks

Introduction

For coal-fired power plants, safety is critical to the success of the business. In general, the quality of steels plays an important role in safety on these plants. These steels need to possess perfect properties because they suffer from severe environmental conditions, such as high temperature, fatigue, and chemical corrosion (Schütze et al., 2004). However, most steels cannot endure such hostile conditions for long periods of time. Their original microstructure deteriorates, leading to a decrease in their mechanical properties (Moakhar et al., 2013). Once the strength of the steel cannot satisfy practical requirements, new cracks are generated in the steel, which give rise to fractures (Toribio et al., 2011). Therefore, the regular and detailed inspection for these steels is a necessary requirement for coal-fired power plants (Gorkunov et al., 2011). Currently, the morphology of spheroidized pearlite is regarded as one important index to evaluate safe levels of the steels (Kim & Kim, 2000; Skowronek et al., 2004; Wang et al., 2012; Ohashi et al., 2013; Yao et al., 2013), by which an inspector can easily determine whether the steels should be changed.

Many investigations have been performed to evaluate the lamellar structure of spheroidized pearlite, and several two-dimensional models have been proposed to investigate the properties of spheroidized pearlite (Brooks, 2000; Nutal et al., 2010; Fu et al., 2014). Recently, a quantitative three-dimensional method was used to observe the morphology of spheroidized pearlite, which provided a new method to track the evolutionary tendency of pearlite spheroidization (Wang et al., 2010). On the other hand, shapes of the spheroidized pearlites were also investigated by their topological or differential-geometric features (Wang et al., 2012). However, in the industrial environment, a simple and fast measurement is very important to prevent accidents. Therefore, for pearlite spheroidization of steels used in coal-fired power plants, Chinese national standards are set to provide an operable procedure for inspectors to determine pearlite spheroidization grades by analyzing shapes of spheroidized pearlites (DL/T674-2001 C.E.P.I.S., 2001; DL/T773-2001 C.E.P.I.S., 2001; DL/T787-2001 C.E.P.I.S., 2001). However, pearlites are very complicated and have no uniform shapes. The standards only offer representative optical metallography images and some qualitative sentences as criteria to determine each pearlite spheroidization grade. It greatly increases the difficulty and error ratio due to different recognition of the morphologies and sentences in the standards. Several methods used to automatically detect pearlite spheroidization grade have been reported. Liu et al. (2012) employed scanning electron microscopy (SEM) to obtain morphologies of cementite phases in spheroidized pearlites. They calculated the fractal dimension of these cementite phases, with which the strength and pearlite spheroidization grades of 15CrMo steel were evaluated. Yao et al. (2013) applied laser-induced breakdown spectroscopy (LIBS) to study the laser-induced spectra of spheroidized pearlites. They found that pearlite spheroidization grades can be readily identified by principal component analysis of the spectra. However, in most cases, SEM or LIBS

Received June 17, 2015; accepted December 3, 2015
*Corresponding author. yeiji_chen@126.com

measurements cannot be used because some steels could not be cut from the equipment as the examined sample. Hence, nondestructive testing is vital to inspect pearlite spheroidization. Optical metallography imaging is identified as one valid method to characterize microstructural morphology of steel, which is also in accord with the standards. In fact, conventional laminating techniques using a plastic film can easily copy the surface morphology of the examined steel on the worksite. Thereafter, scanning this plastic film by optical microscopy in the laboratory can provide an optical metallography image. In such a case, the optical metallography image can be utilized as a convenient tool to determine the pearlite spheroidization grade in the industrial field. The purpose of this work is to eliminate the effect of subjective factors from manual determination of the pearlite spheroidization grade using optical metallography. For the optical metallography images of the steels used in coal-fired power plants, a novel method combining image mining and artificial neural network (ANN) technology is proposed to achieve automatic detection of the pearlite spheroidization grade.

Methods

Model

A representative optical metallography image of each pearlite spheroidization grade is provided in the standards.

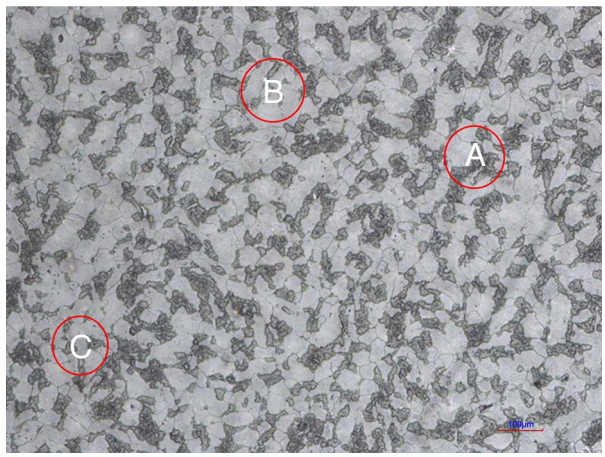

Figure 2. Microstructures of pearlites in the as-received optical metallographic image of ASTM A315-B steel.

Figure 1 shows images of ASTM A315-B steel with different spheroidization grades in the standard. However, the spheroidized pearlites in real images have various shapes that may belong to different spheroidization grades. Figure 2 shows a typical image of ASTM A315-B steel obtained by the laminating technique. The pearlites in the three areas labeled as A, B, and C have very different shapes. Compared with the images in the standard, they belong to 2, 3, and 4

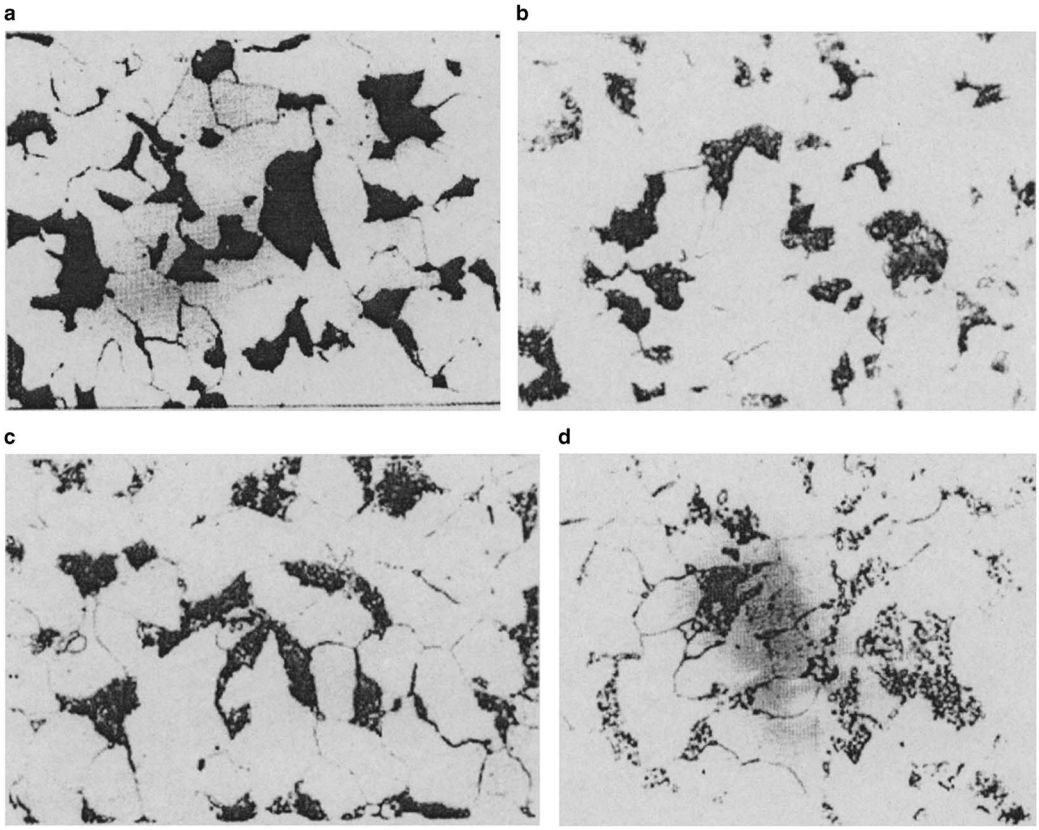

Figure 1. Optical metallography images of (**a**) 1 grade, (**b**) 2 grade, (**c**) 3 grade, (**d**) 4 grade of pearlite spheroidization of ASTM A315-B steel in the standard.

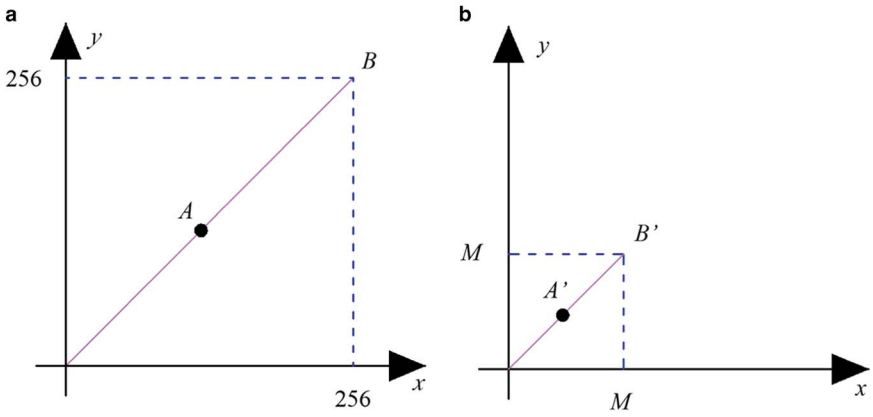

Figure 3. Schematic of gray-level compression from (**a**) the original image to (**b**) the compressed image.

spheroidization grades, respectively. Hence, a comprehensive analysis for all the spheroidized pearlites should be performed before judging the spheroidization grade. For an image, inspectors first estimate percentages of different spheroidization grades, and then determine a suitable spheroidization grade based on the percentage distribution. However, many qualitative judgments, due to variation in personal opinions, can seriously affect the final decision. Hence, automatic detection techniques become an important approach to eliminate the influence of subjective factors during manually determining the spheroidization grade.

In order to simulate the process of determining the pearlite spheroidization grade, a mathematical model needs to be established to calculate the percentages of different pearlite spheroidization grades. Therein, all the pearlites in an image should be classified into the corresponding spheroidization grades. However, there is only one image of each spheroidization grade in the standard. This information is not sufficient to estimate a large number of irregular-shaped pearlites in the images, which makes it more difficult to detect the spheroidization grade. In addition, describing the shape of pearlites by the equations is not easy. Therefore, it appears to be a great challenge to automatically detect the spheroidization grade by comparing the observed carbide morphology with the given carbide morphology in the standard.

There are two problems that need to be addressed for achieving automatic detection of the spheroidization grade. First, the morphology of pearlite can be characterized by several parameters, and then the relationship between these parameters and the spheroidization grade can be established. In this work, we propose a novel method combining image mining and ANN to solve these two problems. A simple way is to eliminate establishing complicated mathematical models used to describe the shape of pearlite. If the optical metallography image containing various shapes of pearlites is only regarded as a normal image without considering the material properties implied in the image, automatic detection of the spheroidization grade becomes a conventional image classification procedure. It is well known that image mining techniques can easily distinguish or classify different images by characteristic parameters that can fully denote the examined image (Fayyad et al., 1996). In this work, all of the as-received images were first calculated to obtain their characteristic parameters using image mining, and then we established the mathematical relationship between these characteristic parameters and the corresponding spheroidization grade. Therein, the spheroidization grade of each image should be known. In this work, the spheroidization grade of each as-received image was ascertained via co-determination based on an expert team consisting of experienced inspectors. Current standards only present spheroidization grades in increments of 1.0. In order to further improve the accuracy, the subdivision method was employed by decreasing the increment from 1.0 to 0.5 according to the standards and experiences of the sophisticated inspectors. Considering the fact that there is not an obvious physical determinant between these characteristic parameters and the spheroidization grade, the numerical fitting method can be used to evaluate their relationship. Currently, ANN is a valid way to fit the mathematical relationships, especially for multiple-input and multiple-output systems (Bhadeshia, 1999), which are different from the conventional material-behavior-evaluation

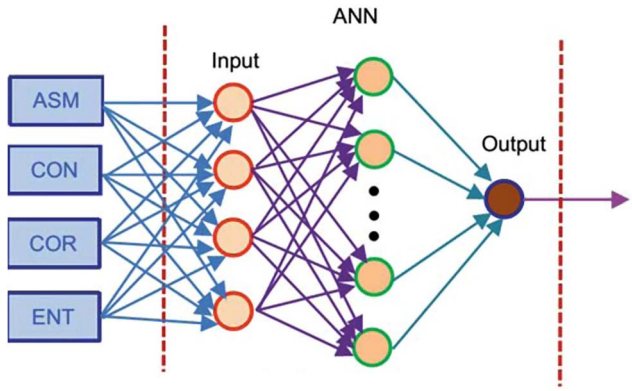

Figure 4. Schematic of automatic detection of pearlite spheroidization grade by the artificial neural networks (ANN) model. ASM, angular second moment; CON, contrast; COR, correlation; ENT, entropy.

Table 1. Chemical Composition of the Three Examined Steels.

Materials	C	Mn	Si	Mo	V	Cr	S	P
ASTM A315-B	0.17–0.24	0.35–0.65	0.17–0.37	—	—	≤0.25	≤0.035	≤0.035
ASTM A335-P12	0.12–0.18	0.40–0.70	0.17–0.35	0.40–0.55	—	0.80–1.10	≤0.030	≤0.030
ASTM A355-P11	0.08–0.15	0.40–0.70	0.17–0.37	0.25–0.35	0.15–0.30	—	≤0.035	≤0.035

techniques (Mandal et al., 2009; Das et al., 2013). Furthermore, many quantitative mathematical models are established using the combination of both image analysis and ANN, with which the problems presented in the industrial field have been successfully resolved (Buessler et al., 2014; Poonnoy et al., 2014; Samtas, 2014).

In this work, characteristic parameters of each as-received image are first calculated by image mining. The mathematical

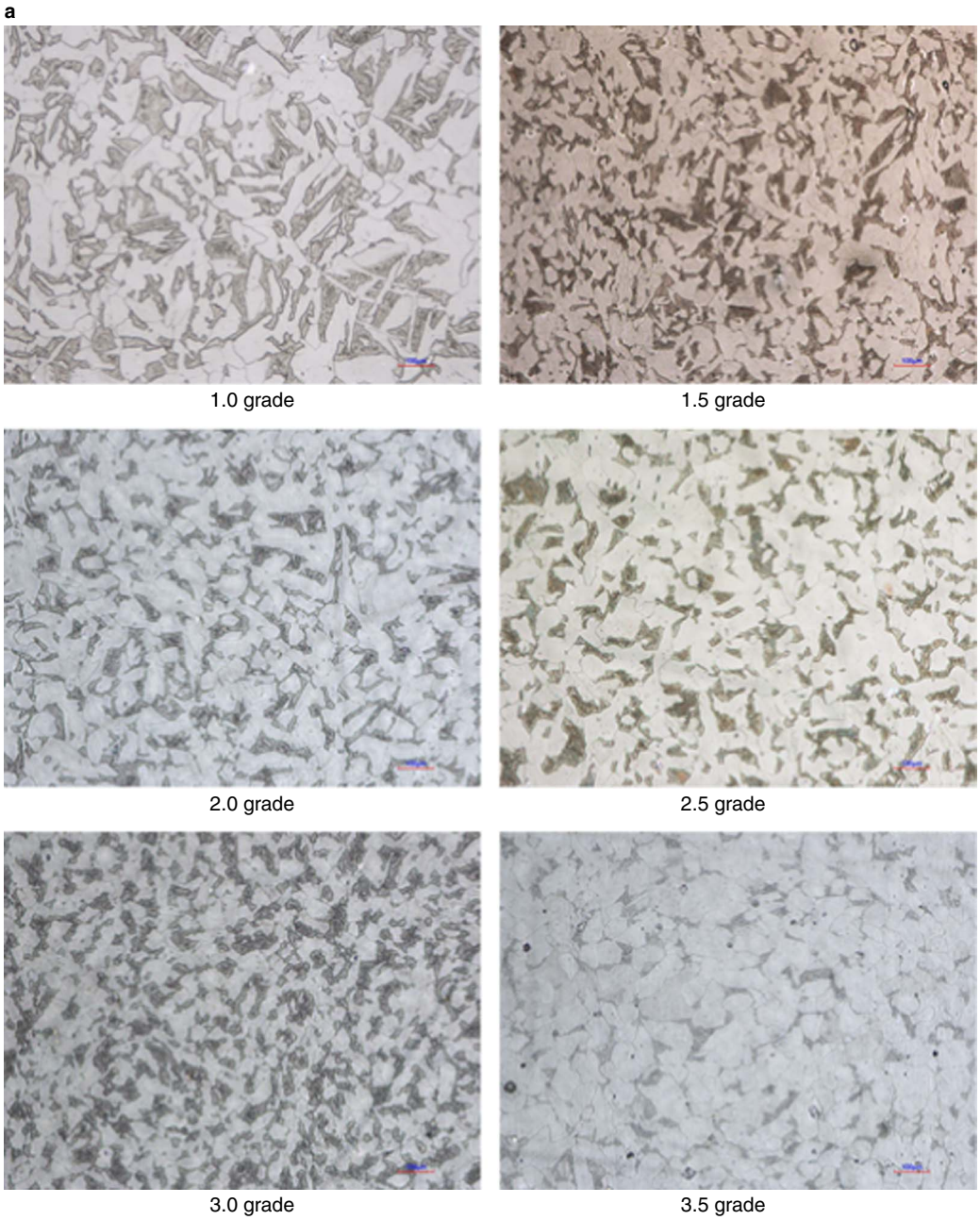

Figure 5. (Continued).

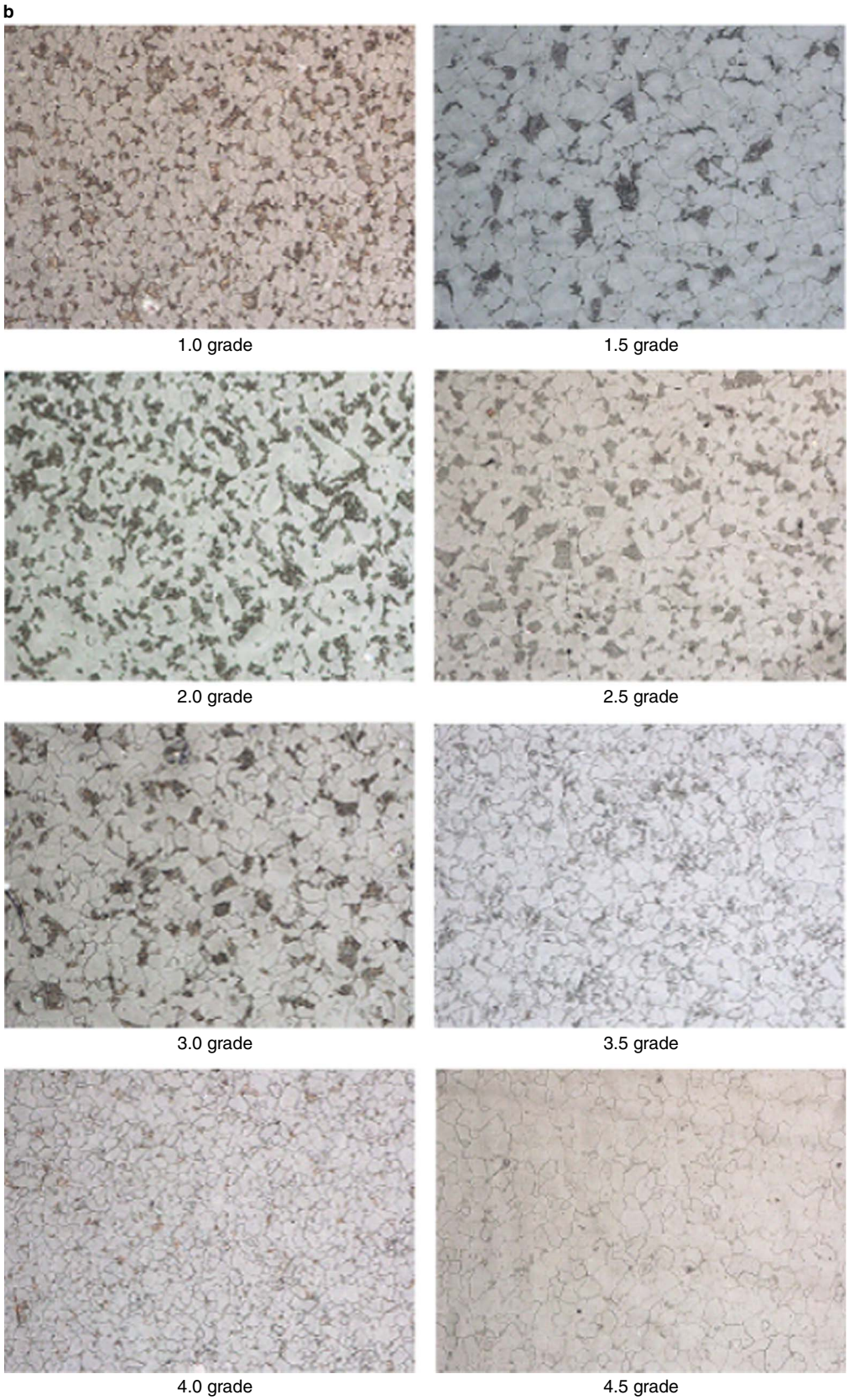

Figure 5. (Continued).

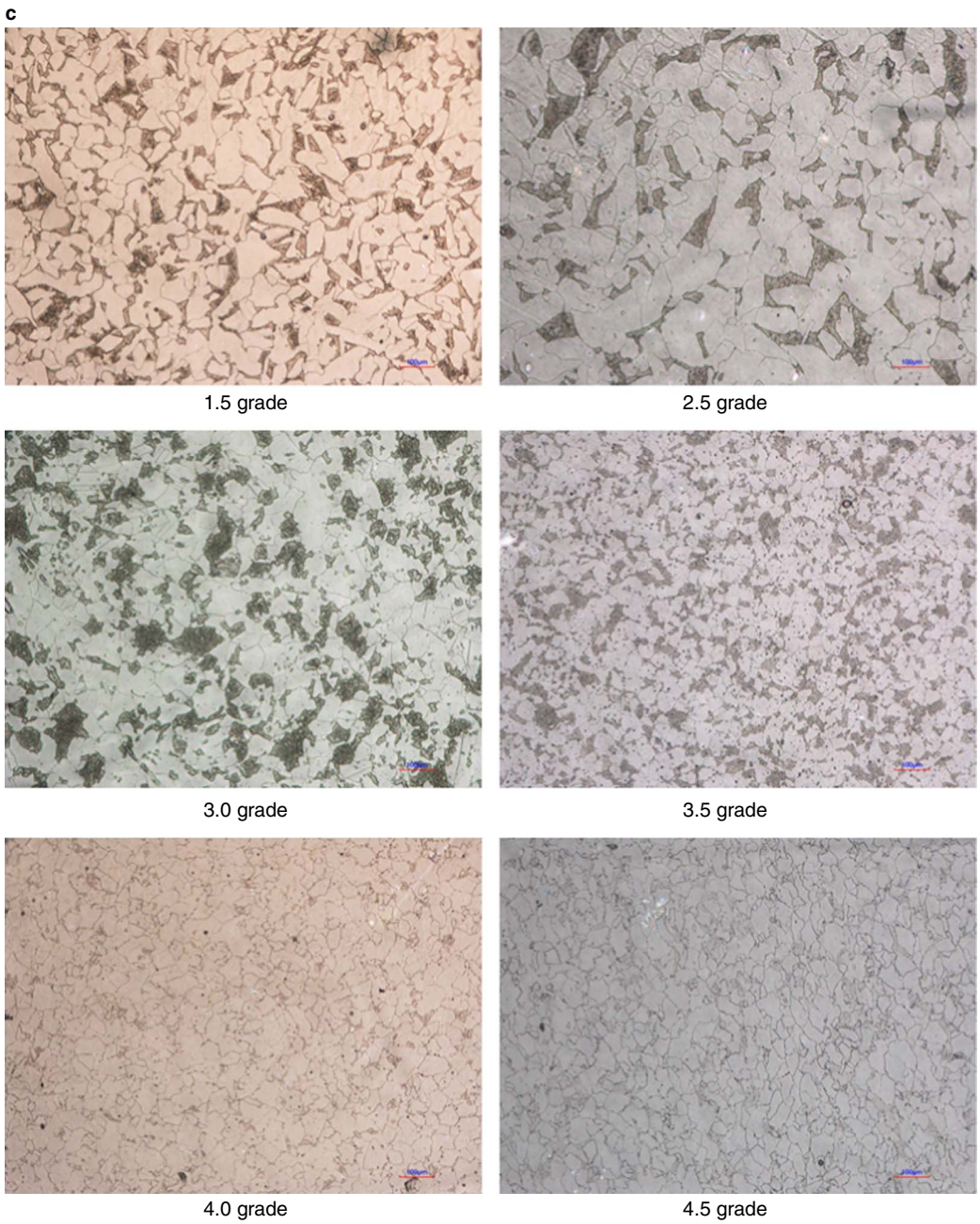

Figure 5. Optical metallography images of (**a**) ASTM A315-B steel, (**b**) ASTM A335-P12 steel, and (**c**) ASTM A355-P11 steel.

model between the characteristic parameters and the corresponding spheroidization grade is established by ANN. Then the spheroidization grade of the examined image can be automatically detected by this ANN model using these characteristic parameters as its input.

Image Mining

The characteristic parameters are carried out by image texture theory. Among them, the gray-level co-occurrence matrix method is often used to distinguish the difference in the texture of images via spatial relations of similar gray tones (Haralick et al., 1973). A subset of data can be derived from a normalized co-occurrence matrix, i.e. angular second moment (ASM), contrast (CON), correlation (COR), and entropy (ENT). In this work, they are selected as the characteristic parameters to denote the examined image. Their expressions are described as follows:

$$\mathrm{ASM} = \sum_{i}\sum_{j} p[i,j]^2, \tag{1}$$

$$\mathrm{CON} = \sum_{n=0}^{N-1} n^2 \left\{ \sum_{i=1}^{N}\sum_{j=1}^{N} p[i,j] \right\}, \text{ where } |i-j| = n, \tag{2}$$

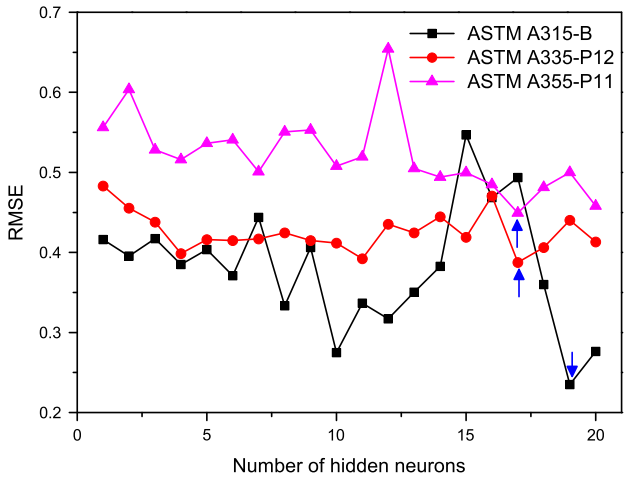

Figure 6. Root mean square error (RMSE) of the artificial neural network model with different numbers of hidden neurons.

$$\mathrm{COR} = \frac{\sum_{i=1}^{N}\sum_{j=1}^{N}(i\times j)\ p[i,\ j] - \mu_x\mu_y}{\sigma_x\sigma_y}, \tag{3}$$

$$\mathrm{ENT} = -\sum_{i}\sum_{j} p[i,\ j]\log(p[i,\ j]), \tag{4}$$

where $p[i,\ j]$ is the $[i,\ j]$th entry in a gray-tone spatial dependence matrix, and N is the number of distinct gray levels in the quantized image. The expected values μ_x and μ_y can be calculated from the following equations:

$$\mu_x = \sum_{i=1}^{N}\sum_{j=1}^{N} i\times p[i,\ j], \tag{5}$$

$$\mu_y = \sum_{i=1}^{N}\sum_{j=1}^{N} j\times p[i,\ j]. \tag{6}$$

The standard deviations σ_x and σ_y can be derived from the following equations:

$$\sigma_x = \sum_{i=1}^{N}\sum_{j=1}^{N} (i-\mu_x)^2\times p[i,\ j], \tag{7}$$

$$\sigma_y = \sum_{i=1}^{N}\sum_{j=1}^{N} \left(j-\mu_y\right)^2\times p[i,\ j]. \tag{8}$$

In addition, compressing the image is convenient to reduce the resource usage and transmission capacity (Tamura et al., 1978). In this work, gray-level compression is carried out for all examined images as follows:

$$\boldsymbol{K}[i,\ j] = \begin{cases} t-1, & \text{if } (t-1)\times M \le \boldsymbol{I}[i,\ j] \text{ and} \\ & \boldsymbol{I}[i,\ j] \le (t-1)\times M + (M-1),\ t\in(1,\ M), \\ \boldsymbol{I}[i,\ j], & \text{otherwise} \end{cases} \tag{9}$$

where i and j are the spatial position in the image $\boldsymbol{I}$ with 256 gray levels, M is the constant obtained by the function of int (256/N), Image $\boldsymbol{K}$ is the new image with M gray levels derived from the grayscale value of image $\boldsymbol{I}$. Figure 3 shows the schematic of the gray-level compression. Pixel A in the image, which has 256 gray levels, can be transferred to pixel A' in the compressed image that has M gray levels. Meanwhile, the relative position of pixel A' in the image does not change after this compression, i.e. the value of OA/AB is equal to that of $OA'/A'B$. This aims to avoid excessive loss of original image information before and after the mathematical process by Equation (9).

Then, the $n_1\times m_1$ co-occurrence matrix $\boldsymbol{T}$ (Haralick et al., 1973; Haralick & Shapiro, 1992) is defined using the $n_2\times m_2$ matrix $\boldsymbol{K}$, parameterized by an offset $(\Delta x,\ \Delta y)$, as

$$\boldsymbol{T}[i,\ j] = \sum_{p=1}^{n_2}\sum_{q=1}^{m_2}\begin{cases} 1, & \text{if } \boldsymbol{K}[p,\ q] = i \text{ and } \boldsymbol{K}[p+\Delta x,\ q+\Delta y] = j \\ 0, & \text{otherwise} \end{cases}, \tag{10}$$

where i and j are the image intensity value of the image, p and q are the spatial position in the image $\boldsymbol{K}$ and the offset $(\Delta x,\ \Delta y)$ is related to the direction used for angle θ and the distance at which d is computed. Here, the N, n_1, m_1, and d are set to be 16, 16, 16, and 1, respectively. Four different directions are selected to impose the synthetic function by normalized method, which is to increase the accuracy. The angles of θ are set to be 0, 45, 90, and 135°, respectively. The normalized co-occurrence matrix $\boldsymbol{p}$ can be derived by the following equation:

$$\boldsymbol{p}_n[i,\ j] = \frac{T_n[i,\ j]}{\sum_{\alpha=1}^{n_1}\sum_{\beta=1}^{m_1} T_n(\alpha,\ \beta)},\ n = 1, 2, 3, 4. \tag{11}$$

Then four groups of the parameters of ASM, CON, COR, and ENT can be carried out by Equations (1)–(11).

Table 2. Average Absolute Relative Error (AARE) and Root Mean Square Error (RMSE) of Artificial Neural Network (ANN) Algorithm for the Training and Test Data.

	ASTM A315-B		ASTM A335-P12		ASTM A355-P11	
Algorithm	AARE (%)	RMSE	AARE (%)	RMSE	AARE (%)	RMSE
During training						
ANN	13.44	0.23	14.86	0.39	14.54	0.45
During testing						
ANN	14.03	0.27	16.73	0.42	17.16	0.41

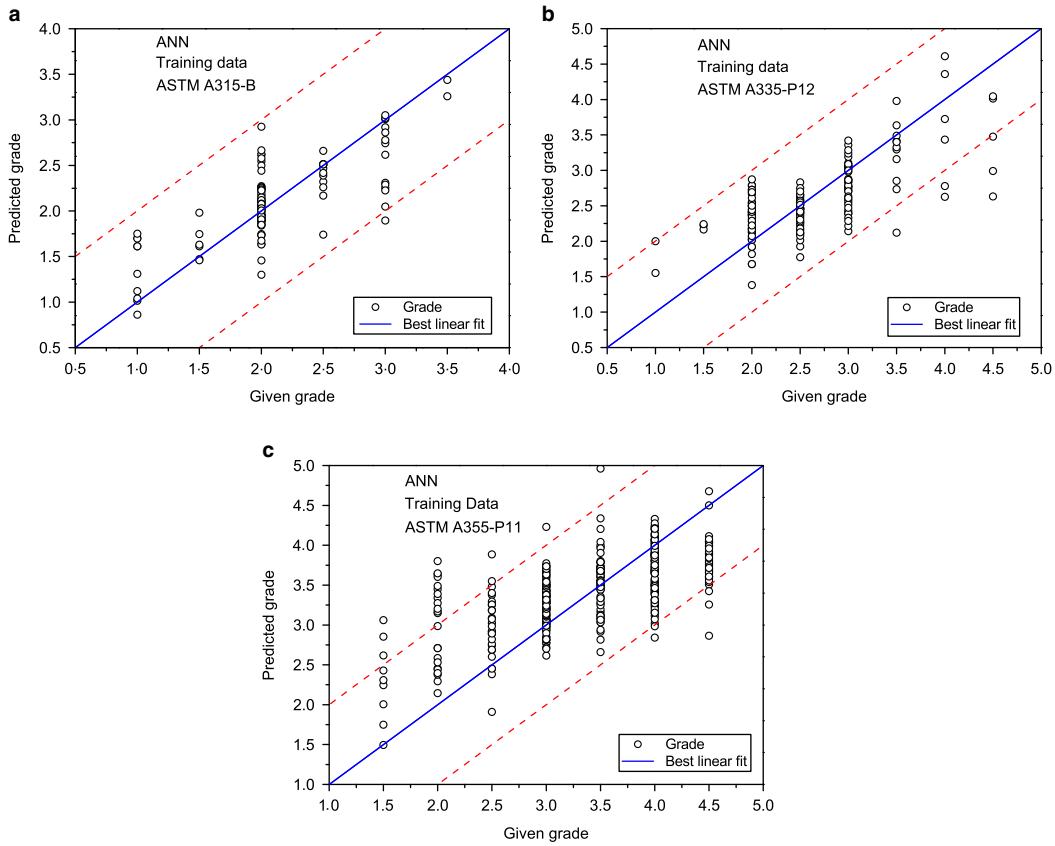

Figure 7. The predicted pearlite spheroidization grades of (**a**) ASTM A315-B steel, (**b**) ASTM A335-P12, and (**c**) ASTM A355-P11 versus the given training data. Red dashed line is parallel to best linear fit with the distance of ±1 grade. ANN, artificial neural networks.

The respective arithmetic mean of these calculated four groups is set as the terminal values of ASM, CON, COR, and ENT for the following usage.

ANN Model

ANN is often used to solve tasks that are hard to solve by ordinary rule-based programming, including machine learning and pattern recognition. ANNs can compute values from inputs by feeding information through the network. In this work, the backpropagation (BP) method (Rumelhart et al., 1986) is applied to train to establish the mathematical relationship between the given spheroidization grade (output) and the four calculated data of ASM, CON, COR, and ENT (inputs). Note that a three-layer ANN model with sigmoid transfer can satisfy any required function in practical applications (Hornik et al., 1989). In this analysis, one hidden layer is applied for the ANN model in this work. A feed-forward BP network model would be formed. In order to obtain the optimal BP model, the optimization method is performed by varying parameters, connection weights, or specifics of the architecture such as the number of neurons or their connectivity. Figure 4 shows the schematic of our proposed method for automatic detection of spheroidization grade from optical metallography images.

Results and Discussion

Based on the above mathematical process, a novel method is proposed by the combination of both image mining and ANN. In this work, three common metal materials of ASTM A315-B steel, ASTM A335-P12 steel, and ASTM A355-P11 steel used in coal-fired power plants were selected as the samples. Their chemical compositions are listed in Table 1. The training data has 106, 154, and 377 images, respectively. On the other hand, test data were also provided to evaluate the validity of the model. In this work, the number of testing images is set as 52 for each examined material. Figure 5 shows some images of these three materials. The results show that these images present a clear difference in ASM, CON, COR, and ENT (this work does not give the values). Then, the feed-forward BP network is trained by the input and output data.

A standard statistical performance evaluation is conducted to obtain the optimal ANN model. The predictability of this algorithm is examined by average absolute relative error (AARE) and average root mean square error (RMSE) (Srinivasulu & Jain, 2006). They can be expressed as

$$\mathrm{AARE}\,(\%) = \frac{1}{N}\sum_{i=1}^{N}\left|\frac{P_i - G_i}{P_i}\right| \times 100, \qquad (12)$$

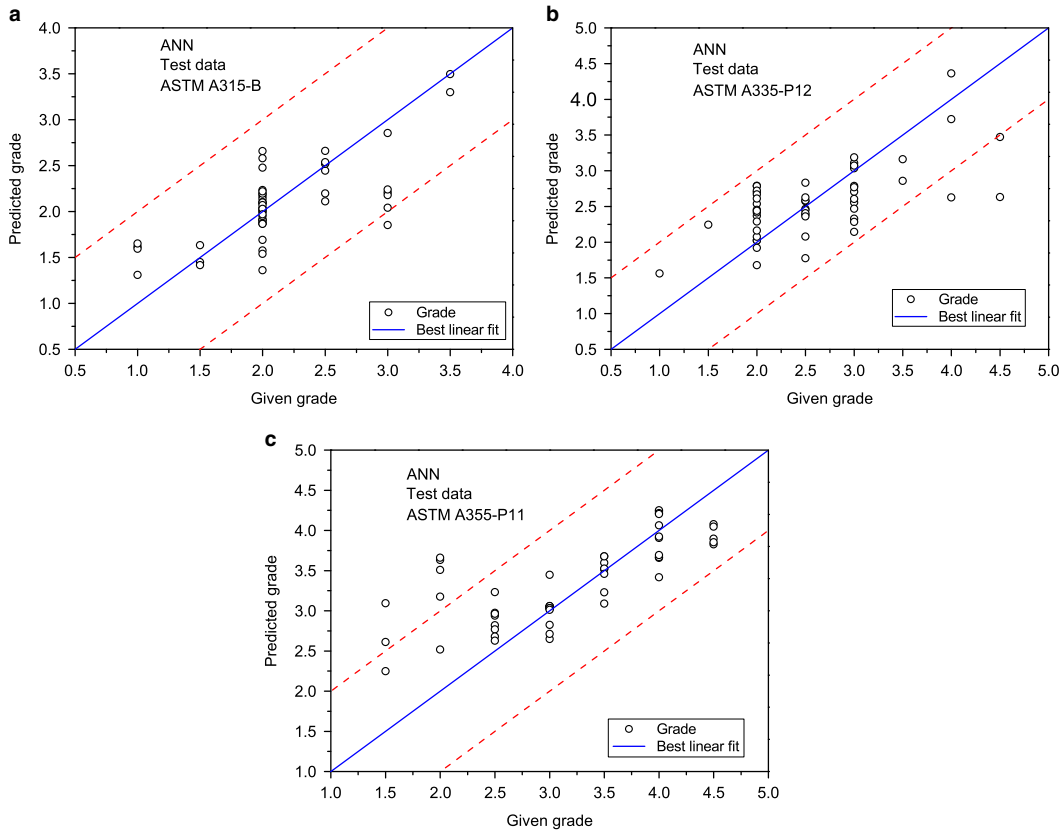

Figure 8. The predicted pearlite spheroidization grades of (**a**) ASTM A315-B steel, (**b**) ASTM A335-P12 steel and (**c**) ASTM A355-P11 steel versus the given test data. Red dashed line is parallel to best linear fit with the distance of ±1 grade. ANN, artificial neural networks.

$$\mathrm{RMSE} = \frac{1}{N}\sum_{i=1}^{N}\left[\sum_{j=1}^{p}\left(G_{ij}-P_{ij}\right)^2\right]^{1/2}, \qquad (13)$$

where G is the given grade and P the predicated value derived from the ANN model. N is the total number of data and p the number of outputs (in this work $p = 1$).

For the ANN model, the number of hidden neurons should be first ascertained before BP algorithm is used. The first layer has four input neurons (ASM, CON, COR, and ENT) that send data via synapses to the second layer with a different number of hidden neurons, and then via more synapses to the third layer with one output neuron (spheroidization grade). In this work, the number of hidden neurons varies from one to 20 to find the optimal model that has the smallest RMSE. The maximum epoch is set to 100, and the error is <0.00004. After the traversal trials, the RMSE of the ANN model of these three materials with different numbers of hidden neurons are shown in Figure 6. It was found that networks with 19, 17, and 17 hidden neurons have the smallest RMSE for the ASTM A315-B, ASTM A335-P12, and ASTM A355-P11 steels, respectively.

For the training and test data of the three examined materials, Table 2 lists the AARE and RMSE of the optimal ANN models. Figures 7 and 8 show the predicted spheroidization grades versus the given spheroidization grades. Here, it should be pointed out that the number of images with the lowest or highest spheroidization grades is far less than those with the intermediate spheroidization grades. The reason for this uneven distribution results from the actual situation. The new or short-run steels are often safe, and they have low spheroidization grades. Consequently, there is no need for sampling and inspecting of this type of material or its spheroidization grade. On the other hand, steels with high spheroidization grades are very dangerous. Hence, before reaching this high spheroidization grade, this steel should be replaced by new steel to avoid the occurrence of accidents. The results show that the ANN algorithm fits all the training and test data well, including the images with the lowest and highest spheroidization grades.

Furthermore, performance of the ANN models is also evaluated by statistical error analysis. The absolute error is employed and carried out by comparing the calculated data with the given data. It is expressed as

$$\text{Absolute error} = |G-P|, \qquad (14)$$

where G and P have the same meaning as described above. Table 3 lists all the absolute errors of these three ANN models. For the training data, the ANN model presents the perfect performance. The accuracies reach 99.05, 95.46, and

Table 3. Accuracies of All the Calculated Spheroidization Grades, Including the Training and Test Data.

Materials	Number of Images	Accuracies Under Different Grade Errors (Δ)					
		$\Delta \leq 0.5$	$0.5 < \Delta \leq 1$	$1 < \Delta \leq 1.5$	$1.5 < \Delta \leq 2$	$2 < \Delta$	$\Delta \leq 1$
During training using ANN							
ASTM A315-B	106	81.13	17.92	0.94	0.00	0.00	99.05
ASTM A335-P12	154	74.03	21.43	3.25	1.30	0.00	95.46
ASTM A355-P11	377	64.19	29.44	4.77	1.59	0.00	93.63
During testing using ANN							
ASTM A315-B	52	78.85	19.23	1.92	0.00	0.00	98.08
ASTM A335-P12	52	65.38	28.85	3.85	1.92	0.00	94.23
ASTM A355-P11	52	75.00	13.46	7.69	3.85	0.00	88.46

ANN, artificial neural networks.

93.63%, respectively, which is also in agreement with the above statistical analysis. For test data, the ANN model also has the performance. The high accuracies of 98.08% (ASTM A315-B steel), 94.23% (ASTM A335-P12 steel), and 88.46% (ASTM A355-P11 steel) make sure that our method is adequate for practically determining the spheroidization grade.

Conclusions

Automatic detection can avoid the effect of subjective factors during manually determining pearlite spheroidization grades of steel using optical metallography microscopy, because inspectors often have a different understanding of the vague descriptions and representative images in the standards. However, the morphology of pearlite is difficult to characterize by a mathematical model, because the pearlites in the images have complicated and irregular shapes. In order to resolve this problem, we abandoned establishing equations to characterize the pearlite. Images containing many pearlites are regarded as the normal image. Then, the conventional image classification method can be applied to achieve the automatic detection of spheroidization grade. Therein, image mining, as a professional technique, can easily distinguish or classify the different images. In this work, a novel method combining image mining and ANN is proposed. Image mining provides the characteristic parameters that can denote the examined image, and ANN is used to establish the simple mathematic model to automatically provide the calculated spheroidization grade according to the characteristic parameters.

In this work, three materials of ASTM A315-B steel, ASTM A335-P12 steel, and ASTM A355-P11 steel commonly used in coal-fired power plants were selected as the samples. The results indicate that the accuracies reach 99.05, 95.46, and 93.63%, respectively, which suggests that our proposed method is adequate for automatically detecting the pearlite spheroidization grade using optical metallography images. In addition, this method and conclusion can also offer a new solution for similar problems of other areas.

Acknowledgments

This work was supported by the National Natural Science Foundation of China under Grant Number 51405285, Innovation Program of Shanghai Municipal Education Commission under Grant Number 15ZZ087, and Science and Technology Commission of Shanghai Municipality under Grant Numbers 14DZ2261000 and 15110501000.

References

Bhadeshia, H. (1999). Neural networks in materials science. *ISIJ Int* **39**, 966–979.

Brooks, C.R. (2000). Microstructural observations of spheroidization from a lamellar structure in iron meteorites. *Mater Charact* **45**, 71–80.

Buessler, J.L., Smagghe, P. & Urban, J.P. (2014). Image receptive fields for artificial neural networks. *Neurocomputing* **144**, 258–270.

Das, A., Sivaprasad, S., Tarafder, M., Das, S.K. & Tarafder, S. (2013). Estimation of damage in high strength steels. *Appl Soft Comput* **13**, 1033–1041.

DL/T674-2001 C.E.P.I.S. (2001). *The Gradational Standard of Spherular Pearlite for Carbon Steel No. 20 used in Fossil Power Plant*. Beijing: China Electric Power Press.

DL/T773-2001 C.E.P.I.S. (2001). *Spheroidization Evaluation Standard of 12Cr1MoV Steel used in Power Plan*. Beijing: China Electric Power Press.

DL/T787-2001 C.E.P.I.S. (2001). *The Gradational Standard of Spherular Pearlite for 15CrMo Steel used in Fossil Power Plant*. Beijing: China Electric Power Press.

Fayyad, U., Piatetsky-Shapiro, G. & Smyth, P. (1996). From data mining to knowledge discovery in databases. *AI Mag* **17**, 37–54.

Fu, Y., Yu, H. & Tao, P. (2014). On-line spheroidization process of medium-carbon low-alloyed cold heading steel. *Int J Min Met Mater* **21**, 26–35.

Gorkunov, E.S., Savrai, R.A., Makarov, A.V., Zadvorkin, S.M. & Malygina, I.Y. (2011). Magnetic inspection of fatigue degradation of a high-carbon pearlitic steel. *Russ J Nondestruct Test* **47**, 803–809.

Haralick, R.M., Shanmugam, K. & Dinstein, I.H. (1973). Textural features for image classification. *IEEE Trans Syst Man Cybern Syst* **SMC-3**, 610–621.

Haralick, R.M. & Shapiro, L.G. (1992). *Computer and Robot* (vol. 1). Boston: Addison-Wesley.

Hornik, K., Stinchcombe, M. & White, H. (1989). Multilayer feedforward networks are universal approximators. *Neural Netw* **2**, 359–366.

Kim, E.S. & Kim, I.S. (2000). Effect of spheroidization on the near-threshold fatigue crack growth in ferrite-pearlite steel. *J Mater Sci Lett* **19**, 367–369.

Liu, C.J., Dung, L.Y. & Jiang, X.D. (2012). Characterizing the spheroidization grade and strength of 15CrMo steel through determining fractal dimension. *Chin J Mech Eng* **25**, 826–831.

Mandal, S., Sivaprasad, P.V., Venugopal, S. & Murthy, K.P.N. (2009). Artificial neural network modeling to evaluate and predict the deformation behavior of stainless steel type AISI 304L during hot torsion. *Appl Soft Comput* **9**, 237–244.

Moakhar, R.S., Mehdipour, M., Ghorbani, M., Mohebali, M. & Koohbor, B. (2013). Investigations of the failure in boilers economizer tubes used in power plants. *J Mater Eng Perform* **22**, 2691–2697.

Nutal, N., Gommes, C.J., Blacher, S., Pouteau, P., Pirard, J.P., Boschini, F., Traina, K. & Cloots, R. (2010). Image analysis of pearlite spheroidization based on the morphological characterization of cementite particles. *Image Anal Stereol* **29**, 91–98.

Ohashi, T., Roslan, L., Takahashi, K., Shimokawa, T., Tanaka, M. & Higashida, K. (2013). A multiscale approach for the deformation mechanism in pearlite microstructure: Numerical evaluation of elasto-plastic deformation in fine lamellar structures. *Mater Sci Eng A* **588**, 214–220.

Poonnoy, P., Yodkeaw, P., Sriwai, A., Umongkol, P. & Intamoon, S. (2014). Classification of boiled shrimp's shape using image analysis and artificial neural network model. *J Food Process Eng* **37**, 257–263.

Rumelhart, D.E., Hinton, G.E. & Williams, R.J. (1986). Learning representations by back-propagating errors. *Nature* **323**, 533–536.

Samtas, G. (2014). Measurement and evaluation of surface roughness based on optic system using image processing and artificial neural network. *Int J Adv Manuf Tech* **73**, 353–364.

Schütze, M., Schorr, M., Renusch, D.P., Donchev, A. & Vossen, J.P.T. (2004). The role of alloy composition, environment and stresses for the oxidation resistance of modern 9% Cr steels for fossil power stations. *Mater Res* **7**, 111–123.

Skowronek, T., Ratuszek, W., Chrusciel, K., Czarski, A., Satora, K. & Wiencek, K. (2004). Spheroidization of cementite in pearlite. *Arch Met Mater* **49**, 961–971.

Srinivasulu, S. & Jain, A. (2006). A comparative analysis of training methods for artificial neural network rainfall–runoff models. *Appl Soft Comput* **6**, 295–306.

Tamura, H., Mori, S. & Yamawaki, T. (1978). Textural features corresponding to visual perception. *IEEE Trans Syst Man Cybern Syst* **SMC-8**, 460–473.

Toribio, J., Gonzalez, B. & Matos, J.C. (2011). Influence of the microstructure of eutectoid steel on the cyclic crack propagation: Pearlite and spheroidite. *Int J Fract* **171**, 209–215.

Wang, Y.T., Adachi, Y., Nakajima, K. & Sugimoto, Y. (2010). Quantitative three-dimensional characterization of pearlite spheroidization. *Acta Mater* **58**, 4849–4858.

Wang, Y.T., Adachi, Y., Nakajima, K. & Sugimoto, Y. (2012). Topology and differential geometry-based three-dimensional characterization of pearlite spheroidization. *ISIJ Int* **52**, 697–703.

Yao, S.C., Dong, M.R., Lu, J.D., Li, J. & Dong, X. (2013). Correlation between grade of pearlite spheroidization and laser induced spectra. *Laser Phys* **23**, 125702.